A Monte Carlo investigation of Swank noise for thick, segmented, crystalline scintillators for radiotherapy imaging

Yi Wang,[a] Larry E. Antonuk,[b] Youcef El-Mohri, and Qihua Zhao
Department of Radiation Oncology, University of Michigan, Ann Arbor, Michigan 48109

(Received 18 November 2008; revised 3 April 2009; accepted for publication 6 April 2009; published 15 June 2009)

Thick, segmented scintillating detectors, consisting of 2D matrices of scintillator crystals separated by optically opaque septal walls, hold considerable potential for significantly improving the performance of megavoltage (MV) active matrix, flat-panel imagers (AMFPIs). Initial simulation studies of the radiation transport properties of segmented detectors have indicated the possibility of significant improvement in DQE compared to conventional MV AMFPIs based on phosphor screen detectors. It is therefore interesting to investigate how the generation and transport of secondary optical photons affect the DQE performance of such segmented detectors. One effect that can degrade DQE performance is optical Swank noise (quantified by the optical Swank factor I_{opt}), which is induced by depth-dependent variations in optical gain. In this study, Monte Carlo simulations of radiation and optical transport have been used to examine I_{opt} and zero-frequency DQE for segmented CsI:Tl and BGO detectors at different thicknesses and element-to-element pitches. For these detectors, I_{opt} and DQE were studied as a function of various optical parameters, including absorption and scattering in the scintillator, absorption at the top reflector and septal walls, as well as scattering at the side surfaces of the scintillator crystals. The results indicate that I_{opt} and DQE are only weakly affected by absorption and scattering in the scintillator, as well as by absorption at the top reflector. However, in some cases, these metrics were found to be significantly degraded by absorption at the septal walls and scattering at the scintillator side surfaces. Moreover, such degradations are more significant for detectors with greater thickness or smaller element pitch. At 1.016 mm pitch and with optimized optical properties, 40 mm thick segmented CsI:Tl and BGO detectors are predicted to provide DQE values of ~29% and 42%, corresponding to improvement by factors of ~29 and 42, respectively, compared to that of conventional MV AMFPIs.
[DOI: 10.1118/1.3125821]

Key words: megavoltage imaging, Monte Carlo simulation, flat-panel imager, segmented scintillators, optical Swank noise, DQE

I. INTRODUCTION

Megavoltage (MV) active matrix, flat-panel imagers (AMFPIs) are routinely used for verifying patient positioning in radiation treatment rooms[1] and are being investigated for cone-beam computed tomography (CBCT).[2] However, the performance of conventional MV AMFPIs is severely limited by the very low (~2%) quantum efficiency (QE) of their x-ray detector, which consists of a copper plate and a phosphor screen. As a result, the detective quantum efficiency (DQE) for conventional MV AMFPIs is only ~1%,[3] which is much lower than that for kilovoltage AMFPIs (~40% to 80%).[4–6] In order to significantly improve portal imaging performance,[7] as well as reduce the dose requirement for MV CBCT imaging,[7–9] it is necessary to substantially increase the DQE of MV AMFPIs.

Toward achieving significantly increased DQE, various forms of high-efficiency x-ray detectors have been theoretically and empirically examined by many research groups. These detectors are based on concepts involving high pressure gas (e.g., xenon) chambers employing tungsten walls,[10–12] thick optical fibers detecting Cerenkov radiation,[13] thick HgI_2 photoconductors,[14] segmented phosphors based on photopolymer matrices,[15] and segmented crystalline scintillators which consist of 2D matrices (or 1D arrays) of scintillator crystals separated by optically opaque septal walls.[7,16–19] Among these approaches, segmented crystalline scintillators offer significantly improved QE, with only limited loss in spatial resolution, and possibly no substantial increase in noise compared to conventional AMFPIs. In order to examine this strategy, 1D segmented arrays incorporating zinc tungstate ($ZnWO_4$) and cadmium tungstate ($CdWO_4$) scintillators,[17–19] as well as 2D segmented matrices employing bismuth germanate (BGO), thallium-doped cesium iodide (CsI:Tl) and $CdWO_4$ scintillators,[7,20–22] have been investigated by different research groups. Recently, a 40 mm thick segmented CsI:Tl detector, with an element-to-element pitch of 1.016 mm and an area of 16.25 $\times$ 16.25 cm^2, has been developed and evaluated by our group.[16] A prototype MV AMFPI incorporating this detector exhibited a DQE of ~22% for a 6 MV x-ray beam.[16] However, the construction and performance of this initial prototype were far from optimal.

TABLE I. Glossary of the symbols and abbreviations used in this article.

Performance metrics	
QE	Quantum efficiency
I	Swank factor
I_{rad}	Radiation Swank factor
I_{opt}	Optical Swank factor
DQE	Detective quantum efficiency
DQE_{rad}	Radiation DQE
Distributions	
AED	Absorbed energy distribution
OPD	Optical pulse distribution
PHD	Pulse height distribution
M_i	The ith moment of a distribution
Detector geometric properties	
T_{sci}	Thickness of scintillator crystals
W_{sci}	Width of scintillator crystals
ϕ_{sci}	Aspect ratio of scintillator crystals
P_E	Element-to-element pitch
W_{wall}	Width of septal walls
Functions	
round	Rounding to nearest integers
Poisson	Generating Poisson integers
norm	Normalizing vectors
Detector optical properties	
μ_A	Material absorption coefficient
$\mu_{A\text{-sci}}$	Absorption coefficient: Scintillator
μ_S	Material scattering coefficient
$\mu_{S\text{-sci}}$	Scattering coefficient: Scintillator
α	Surface absorptivity
α_{top}	Absorptivity: Top reflector
α_{wall}	Absorptivity: Septal walls
β	User-selected scalar for roughness
$\vec{n}_0$	Normal to a surface
$\vec{n}_R$	Normal to a local microfacet
$\vec{v}$	Unit vector with random direction
θ	Angular tilt of $\vec{n}_R$ from $\vec{n}_0$
θ_{max}	Surface roughness
$\theta_{max-0.9}$	Roughness resistance
G	Scintillator conversion gain
$G_{CsI:Tl}$	Conversion gain of CsI:Tl
E	Energy deposition in scintillator
N	No. of photons generated per E
E_A	Absorbed energy per X ray
N_G	No. of generated photons per X ray
N_D	No. of detected photons per X ray
N_E	No. of detected photons per MeV
η	Optical detection efficiency
γ	Critical angle: Total internal reflection

The use of computational tools, such as Monte Carlo simulation, to guide the design of these segmented detectors can be of assistance in optimizing their DQE performance, given the complexity of their structures. For example, previous Monte Carlo simulations of radiation transport have indicated that MV AMFPIs employing 10 to 40 mm thick, segmented CsI:Tl and BGO detectors could offer radiation DQE (DQE_{rad}) values ~10 to 50 times higher than the DQE measured from conventional AMFPIs.[7] Encouraged by these early findings, it is interesting to next investigate how the generation and transport of secondary optical photons could affect the DQE performance of AMFPIs employing such segmented detectors.

One optical effect that degrades DQE involves the optical component of Swank noise. Swank noise arises from variations in the pulse height distribution (PHD) – the distribution of the number of optical photons detected for each interacting X ray.[23] This noise has both radiation and optical components. Radiation Swank noise represents the variation in the absorbed energy distribution (AED) – the distribution of the amount of energy absorbed in the scintillator for each interacting X ray. (In this representation, the AED includes any variations in the absorbed energy due to the use of a polyenergetic radiation beam.) Optical Swank noise represents the variation in the optical pulse distribution (OPD) – the distribution of the number of optical photons detected for each unit of energy absorbed in the scintillator. Swank noise and its components are quantified by Swank factors ranging from 0 to 1, with larger values representing lower noise. The total Swank factor (I) may be considered to consist of two main components, both of which degrade DQE: the radiation Swank factor (I_{rad}) and the optical Swank factor (I_{opt}).[23]

In the absence of additive noise and noise power aliasing, the zero-spatial-frequency DQE of an AMFPI may be expressed as follows:[23,24]

$$DQE = QE \times I. \quad (1)$$

In the absence of optical effects, the zero-frequency value of DQE_{rad} is obtained from the product of QE and I_{rad}.[25] In principle, an increase in scintillator thickness will lead to a higher QE (due to greater radiation attenuation) and a larger I_{rad} (due to more complete absorption of the x-ray energy), resulting in a higher DQE_{rad}. However, when scintillator thickness increases, optical photons have to traverse longer pathways, on average, to reach the underlying flat-panel array, which leads to more light loss and thus a smaller I_{opt} – resulting in smaller I. It is anticipated that such decreases in I_{opt} will, at least partially, offset the potential gains in DQE obtained through increasing scintillator thickness.[22]

In this article, Monte Carlo simulations of radiation and optical transport were performed to investigate Swank noise and DQE for MV AMFPIs based on thick, segmented scintillating detectors. This study was conducted as part of a program of research to support the development of such sophisticated, high-efficiency detectors.

II. METHODS

A glossary of the symbols and abbreviations used in this article appears in Table I.

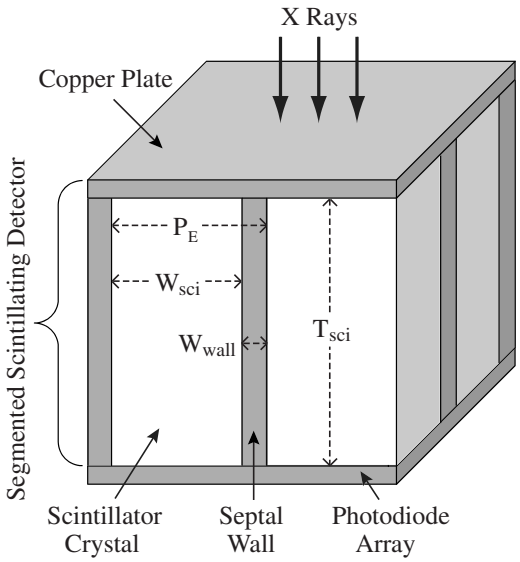

FIG. 1. Three-dimensional schematic drawing, not to scale, of a representative portion of the megavoltage AMFPIs simulated in this study. Each simulated detector consists of a 2D matrix of scintillator crystals, separated by septal walls, with an overlying top copper plate. The detector is coupled to a photodiode array, which is represented in the simulation by a thin layer of silicon. See main text for further details.

II.A. Segmented scintillating detectors

Figure 1 shows a schematic view of a portion of the general structure of the simulated AMFPIs, each of which consists of a segmented scintillating detector coupled to a photodiode array (represented in the simulation by a 0.001 mm thick *a*:Si-H layer). The detector consists of a 1 mm thick copper plate (serving as a radiation build-up layer and a top optical reflector) coupled to the incident x-ray side of the segmented scintillator. The scintillator consists of 81×81 scintillator crystals separated by polystyrene septal walls. The width of the septal walls W_{wall} is 0.05 mm throughout this study. Monte Carlo simulations were performed for a variety of segmented BGO and CsI:Tl detector designs with thicknesses T_{sci} of 10 to 40 mm and element-to-element pitches P_E (the distance between the center of two adjacent crystals) of 0.508 to 1.016 mm. Note that the pixel pitch of the indirect-detection flat-panel array presently being used to evaluate prototype segmented scintillating detectors by our group is 0.508 mm.[26] The aspect ratio of the scintillator crystals, ϕ_{sci}, is defined by

$$\phi_{sci} = \frac{T_{sci}}{W_{sci}} = \frac{T_{sci}}{P_E - W_{wall}}, \tag{2}$$

where W_{sci} is the width of the scintillator crystal.

II.B. Monte Carlo code

A recently implemented Monte Carlo code, MANTIS (v2.0),[27] was used to perform simulations for the determination of QE, I_{rad}, and I_{opt} for MV AMFPIs employing segmented BGO and CsI:Tl detectors. DQE was calculated using Eq. (1) while DQE_{rad} was obtained from the product of QE and I_{rad}. MANTIS is a combination of a radiation transport code (PENELOPE-2005)[28] and an optical transport code (DETECT-II).[29] PENELOPE is employed to simulate the energy deposition for each incident X ray. Once x-ray energy is deposited in a scintillator material, DETECT-II is triggered to generate optical photons which are emitted isotropically. For an energy E deposited in the scintillator crystal, N optical photons are generated using the following expression:

$$N = \text{Poisson}[\text{round}[E \times G]], \tag{3}$$

where Poisson is a function to generate integers with a Poisson distribution, round is a rounding function, and G is the average optical conversion gain of the scintillator material (i.e., 54000 and 8500 photons/MeV for CsI:Tl and BGO, respectively).[30,31] The optical code simulates the transport of each of the N photons. The optical simulation of a photon is terminated once the optical photon is absorbed in the segmented detector or detected by the underlying photodiode array. Each material involved in the simulation was assigned a refractive index, an optical absorption coefficient μ_A, and an optical scattering coefficient μ_S. For simplicity, these and other optical parameters used in the study are assumed to be wavelength independent.

In DETECT-II simulations, optical surfaces can be defined as partially or totally absorptive, with a user-defined surface absorptivity α, which can range from 0 to 1. Optical photons that are not absorbed will be either reflected back to the original medium, or refracted into the next medium. For surfaces allowing light transmission, the code determines if a light photon is reflected or refracted at the surface using Fresnel's law. For surfaces not allowing light transmission (i.e., reflectors), all photons that are not absorbed will be reflected back toward the original medium.

For a smooth surface, the direction of reflected photons is determined using the normal to the surface, $\vec{n}_0$, and the rule for specular reflection. The direction of refracted photons is calculated using $\vec{n}_0$ and Snell's law. As illustrated in Fig. 2, for each optical reflection or refraction occurring at a rough surface S_0, the code calculates a normal $\vec{n}_R$ to a local microfacet S_R having an angle θ with respect to $\vec{n}_0$. The distribution of θ is governed by a user-selected scalar β, which can range from 0 to 1. For each optical interaction, the code generates a unit vector with random direction $\vec{v}$ and calculates $\vec{n}_R$ as follows:

$$\vec{n}_R = \text{norm}[\vec{n}_0 + \beta\vec{v}], \tag{4}$$

where norm is the normalization function for vectors. In this article, surface roughness is expressed in terms of the maximum value of θ, θ_{max}. The correspondence between the selected value of β and θ_{max} is given by

$$\theta_{max} = \arcsin(\beta). \tag{5}$$

In this representation, θ_{max} corresponds to the largest angle between the plane of the local microfacets and the plane determined by S_0. Roughness can be measured by means of extracting a profile of the surface topology from which a distribution of θ angles for local microfacets can be determined. θ_{max} is related to the maximum value of that distribution.

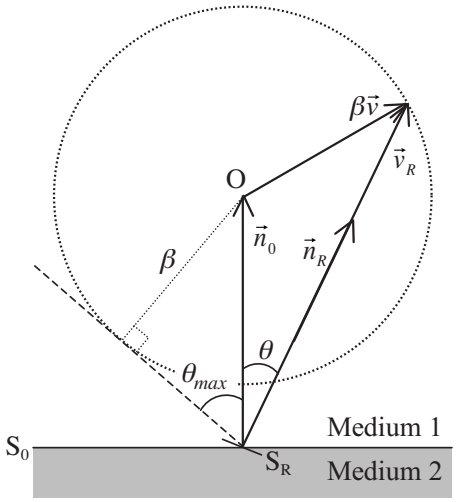

FIG. 2. Illustration of the surface roughness model used by DETECT-II. S_0 is an interface plane adjoining media 1 and 2, and S_R is a local microfacet that is tilted at an angle θ with respect to S_0. The definitions of $\vec{n}_0$, β, $\vec{v}$, and θ_{max} are given in the main text. Note that $\vec{v}_R$ is equal to the vector sum of $\vec{n}_0$ and $\beta\vec{v}$. Since $\vec{v}$ is a unit vector with random direction, the end points of $\vec{v}_R$ are located at points along a dotted circle of radius β, centered at point O. The dashed line, originating from the point of optical interaction, is tangent to the circle. Note that this model can generate nonphysical solutions for which the vector representing the reflected or refracted photon points toward the wrong medium. In such cases, the code will abandon the solution and repeat the calculation by generating a new $\vec{v}$ until a physical solution is obtained.

II.C. Monte Carlo simulations

In this article, the phrase "detector design" will refer to a collection of detector configurations that employ the same scintillator material (i.e., BGO or CsI:Tl) and have the same detector geometry (i.e., T_{sci}, P_E, and W_{wall}). For each detector design, QE and I_{rad} were obtained using a customized version of MANTIS in which optical transport is disabled. For all radiation simulations, the cut-off energies for electrons, positrons, and x-ray photons (the minimum energy below which tracking of a quantum is terminated) were set to a common value of 0.01 MeV. The radiation source was a parallel 6 MV photon treatment beam[32] with an area of 10×10 mm^2. Depending on the element-to-element pitch, 1.016 or 0.508 mm, the beam covers $\sim10\times10$ or 20×20 detector elements, respectively. The beam area is large enough to accurately simulate the effects occurring at the septal walls and small enough compared to detector area to ensure containment of lateral secondary radiation. The choice of a parallel beam over a pencil beam provides better accuracy in the determination of QE and Swank factor. For a given detector design, 10^6 x-ray histories were used in the determination of QE and I_{rad}, whereas, for a given detector configuration, 10^5 histories were used in the determination of I_{opt}. (Simulations involving optical interactions were more computationally intensive and thus necessitated fewer histories.) The simulations reported in this article were performed using a 64-bit Linux cluster with up to two hundred 1.8 GHz AMD Opteron processors and consumed a total of ~350000 CPU hours.

The QE was determined directly from the fraction of the incident X rays that deposit energy in the scintillator crystals (which is a standard output from MANTIS). In addition, a customized output was used to record the energy deposited in the scintillator crystals by each interacting X ray. This information was used to generate the absorbed energy distribution from which I_{rad} is calculated. For selected detector designs, I_{opt} was determined as a function of the various detector optical properties, including absorption and scattering in the scintillator crystals, absorption at the top reflector and at the septal walls, as well as scattering at the side surfaces of the crystals. For the determination of I_{opt}, MANTIS was used to provide the number of optical photons detected as well as the amount of energy absorbed in the scintillator crystals for each interacting X ray. The ratio of these two quantities yielded the number of light photons detected per unit of absorbed energy for each interacting X ray. This number was used to generate the OPD from which I_{opt} was determined.

Each Swank factor (I, I_{rad}, and I_{opt}) was calculated using an expression of the form[23]

$$I = \frac{M_1^2}{M_0 \times M_2}, \tag{6}$$

where M_i is the ith order moment of a distribution $P(x)$ obtained from[33]

$$M_i = \int x^i \times P(x)dx. \tag{7}$$

The refractive indices of BGO, CsI:Tl, and the a:Si-H photodiode were assumed to be 2.15, 1.79, and 1.70, respectively.[30,31] The absorption and scattering coefficients for both BGO and CsI:Tl ($\mu_{A\text{-sci}}$ and $\mu_{S\text{-sci}}$) were assumed to be 0.02 and 0 cm^{-1}, respectively,[34] unless otherwise stated. The assumption of $\mu_{S\text{-sci}}=0$ cm^{-1} corresponds to a scintillator that is perfectly nonscattering. All surfaces were assumed to be smooth, except for the side surfaces of the scintillator crystals whose roughness was defined by the parameter θ_{max} (with θ_{max} ranging from 0° to 30°). The top reflector and septal walls were simulated as reflectors (prohibiting optical transmission) with absorption characterized by absorptivities of α_{top} and α_{wall}, respectively. The bottom surface of the scintillator crystals was assumed to allow light transmission with no optical absorption and all photons passing into the photodiode layer are counted as detected signal. This corresponds to the absence of any optical coupling medium.

The values for the optical parameters investigated in this article correspond to ranges that encompass the estimated values for existing and anticipated segmented scintillators. For example, a recently developed CsI:Tl prototype scintillator,[16] with a thickness of 40 mm and a pitch of 1.016 mm, exhibits an estimated, combined scattering and absorption coefficient of less than 0.02 cm^{-1}. In addition, given a reflectivity of more than ~94% for the septal walls and the fact that the estimated I_{opt} for this prototype is ~0.8,[16] it was estimated that the absorptivity α_{wall} is only a few percentage while θ_{max} is less than ~10°. While these are rough estimates, they nevertheless provide a benchmark for future prototype development.

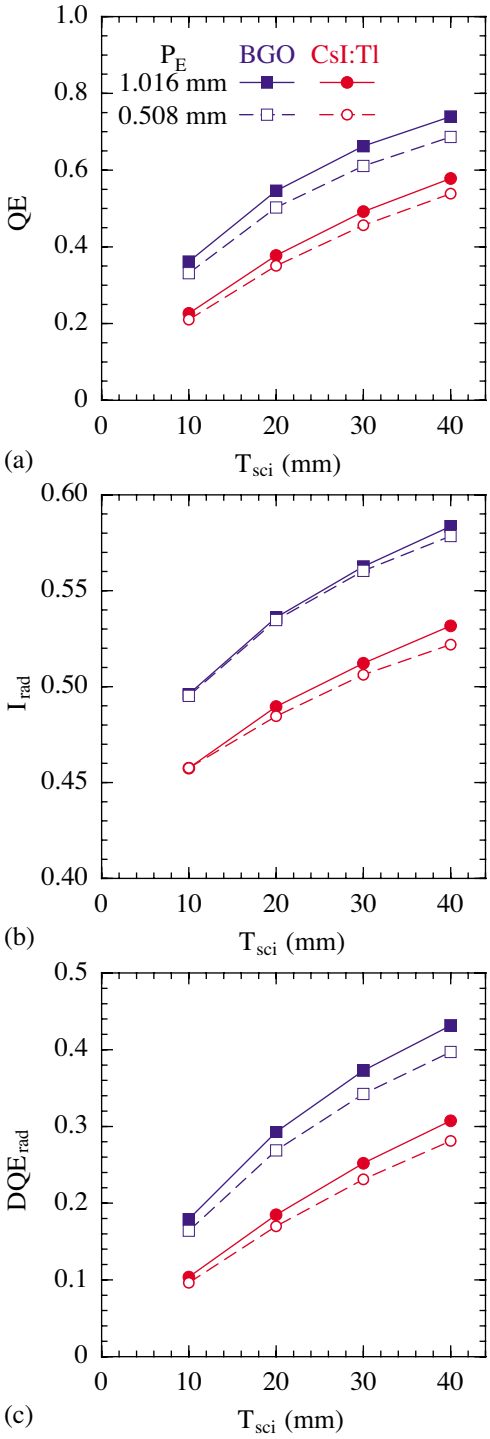

FIG. 3. Simulation results for (a) QE (b) radiation Swank factor (I_{rad}) and (c) radiation DQE (DQE_{rad}). The results are plotted as a function of scintillator thickness T_{sci} for segmented BGO and CsI:Tl detectors at pitches of 1.016 and 0.508 mm. In this and the remaining figures, lines are drawn between the points to guide the eye, unless otherwise indicated.

III. RESULTS

III.A. QE, I_{rad}, and DQE_{rad}

Figure 3 shows results for QE, I_{rad}, and DQE_{rad} as a function of scintillator thickness for AMFPIs employing 10 to 40 mm thick segmented BGO and CsI:Tl detectors with element pitches of 1.016 and 0.508 mm. Detectors with greater T_{sci} and higher scintillator density (i.e., BGO) exhibit higher QE due to increased x-ray attenuation and larger I_{rad} due to more efficient absorption of x-ray energy. Moreover, detectors with larger P_E show slightly higher QE and I_{rad} due to their larger scintillator fill factor (90% at 1.016 mm versus 81% at 0.508 mm). The trends for DQE_{rad} are similar to those for QE and I_{rad}.

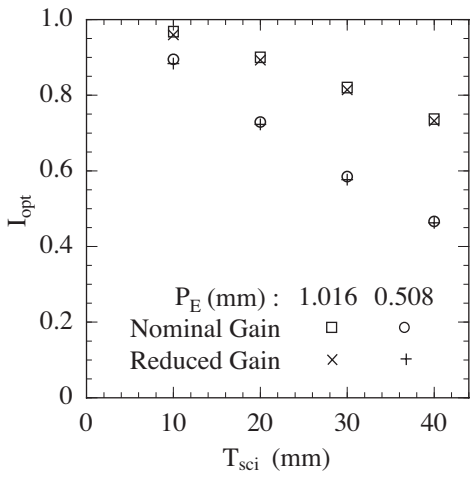

FIG. 4. Simulation results for optical Swank factor (I_{opt}) plotted as a function of T_{sci}. The results were obtained using the nominal and a reduced conversion gain, $G_{CsI:Tl}$ and $0.1 \times G_{CsI:Tl}$, respectively. Results are shown for 10 to 40 mm thick segmented CsI:Tl detectors at pitches of 1.016 and 0.508 mm.

III.B. Validation of the use of reduced conversion gain for CsI:Tl

The amount of computational time required for the intended systematic examination of I_{opt} for CsI:Tl detectors would exceed that available for this study if the nominal conversion gain for that material, $G_{CsI:Tl}$ (54000 photons/MeV), were used. In order to overcome this limitation, a reduced value for conversion gain, $0.1 \times G_{CsI:Tl}$, was used. The conditions under which such a reduction will still lead to a correct determination of I_{opt} are described in the Appendix.

In order to validate the use of this reduction, a comparison of I_{opt} for values determined through simulations of 10 to 40 mm thick CsI:Tl detectors at pitches of 1.016 and 0.508 mm was performed using both $G_{CsI:Tl}$ and $0.1 \times G_{CsI:Tl}$. In these simulations, α_{top}, α_{wall}, and θ_{max} were assumed to be 100%, 4%, and 0°, respectively. The results of the calculations, shown in Fig. 4, demonstrate that the use of reduced gain results in negligible underestimation of I_{opt} for the examined detector designs. Moreover, given these results, it is reasonable to expect that the use of reduced gain should also be valid for CsI:Tl detectors at pitches between 0.508 and 1.016 mm. Reduced gain was therefore used for all remaining CsI:Tl detector simulations. In the case of the BGO detector simulations, a reduction in conversion gain is not required due to the more modest magnitude of that parameter (8500 photons/MeV).

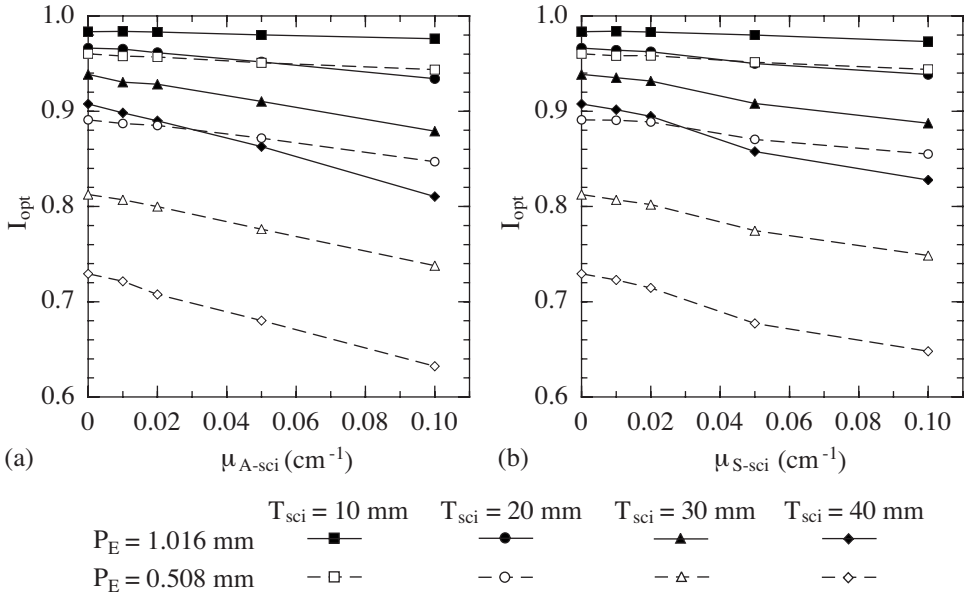

FIG. 5. Simulation results for I_{opt} as a function of (a) scintillator absorption coefficient $\mu_{A\text{-sci}}$ and (b) scintillator scattering coefficient $\mu_{S\text{-sci}}$. Results are shown for 10 to 40 mm thick segmented CsI:Tl detectors at pitches of 1.016 and 0.508 mm.

III.C. I_{opt} and DQE

In this section, simulation results for I_{opt} and DQE are reported as a function of various detector optical properties for selected segmented detector designs. A summary of the comparative behaviors of I_{opt} for the BGO and CsI:Tl detectors appears in Sec. III C 5.

III.C.1. Absorption and scattering in scintillator crystals

Figures 5(a) and 5(b) show results for I_{opt} as a function of $\mu_{A\text{-sci}}$ (assuming $\mu_{S\text{-sci}}$ is 0 cm^{-1}) and $\mu_{S\text{-sci}}$ (assuming $\mu_{A\text{-sci}}$ is 0 cm^{-1}), respectively, for segmented CsI:Tl detectors at various values of T_{sci} and P_E. In these simulations, α_{top}, α_{wall}, and θ_{max} were assumed to be 100%, 2%, and 0°, respectively. The results indicate that I_{opt} decreases with increasing $\mu_{A\text{-sci}}$ and $\mu_{S\text{-sci}}$. Moreover, the rate of decrease is seen to be steeper for detectors with greater thickness but not obviously different for detectors of different pitches. Furthermore, the decline in I_{opt} with increasing $\mu_{A\text{-sci}}$ is found to be approximately linear. [Note that, when both values of $\mu_{A\text{-sci}}$ and $\mu_{S\text{-sci}}$ are concurrently nonzero, the resulting decrease in I_{opt} approximately corresponds to the combined decline observed from the individual dependencies illustrated in Figs. 5(a) and 5(b)]. In addition, for the detector configurations illustrated in Fig. 5, the effects of $\mu_{A\text{-sci}}$ and $\mu_{S\text{-sci}}$ on DQE (which are not shown) are minimal for detectors thinner than 20 mm (i.e., DQE changes by less than 0.008) and are still relatively modest for detectors between 20 and 40 mm thick (i.e., DQE changes by less than 0.03).

In the simulations reported in the remainder of this article, $\mu_{A\text{-sci}}$ and $\mu_{S\text{-sci}}$ are assumed to be fixed at 0.02 and 0 cm^{-1}, respectively, for both BGO and CsI:Tl. These values represent optical properties that are close to those of the CsI:Tl material used in our present detector development efforts.[34] Although BGO is a more transparent material with negligible levels of optical absorption and scattering, the use of the same $\mu_{A\text{-sci}}$ and $\mu_{S\text{-sci}}$ values for both scintillators allows direct comparison of the behavior of the corresponding I_{opt} as a function of other optical properties. Slightly overestimating the value of $\mu_{A\text{-sci}}$ for BGO leads to a small underestimate of I_{opt} and DQE.

III.C.2. Absorption at the top reflector

In Fig. 6, simulation results for I_{opt} are shown as a function of α_{top} for 20 and 40 mm thick segmented BGO and CsI:Tl detectors at pitches of 1.016 and 0.508 mm. In these simulations, α_{wall} and θ_{max} were assumed to be 2% and 0°, respectively. For all examined detector designs, I_{opt} decreases

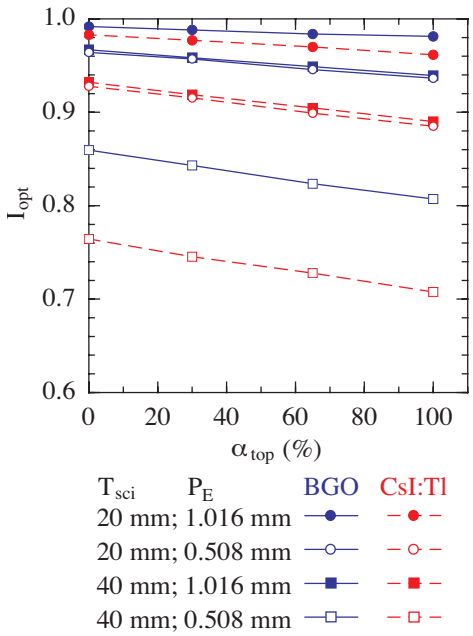

FIG. 6. Simulation results for I_{opt} plotted as a function of top reflector absorptivity α_{top}. Results are shown for 20 and 40 mm thick segmented BGO and CsI:Tl detectors at pitches of 1.016 and 0.508 mm.

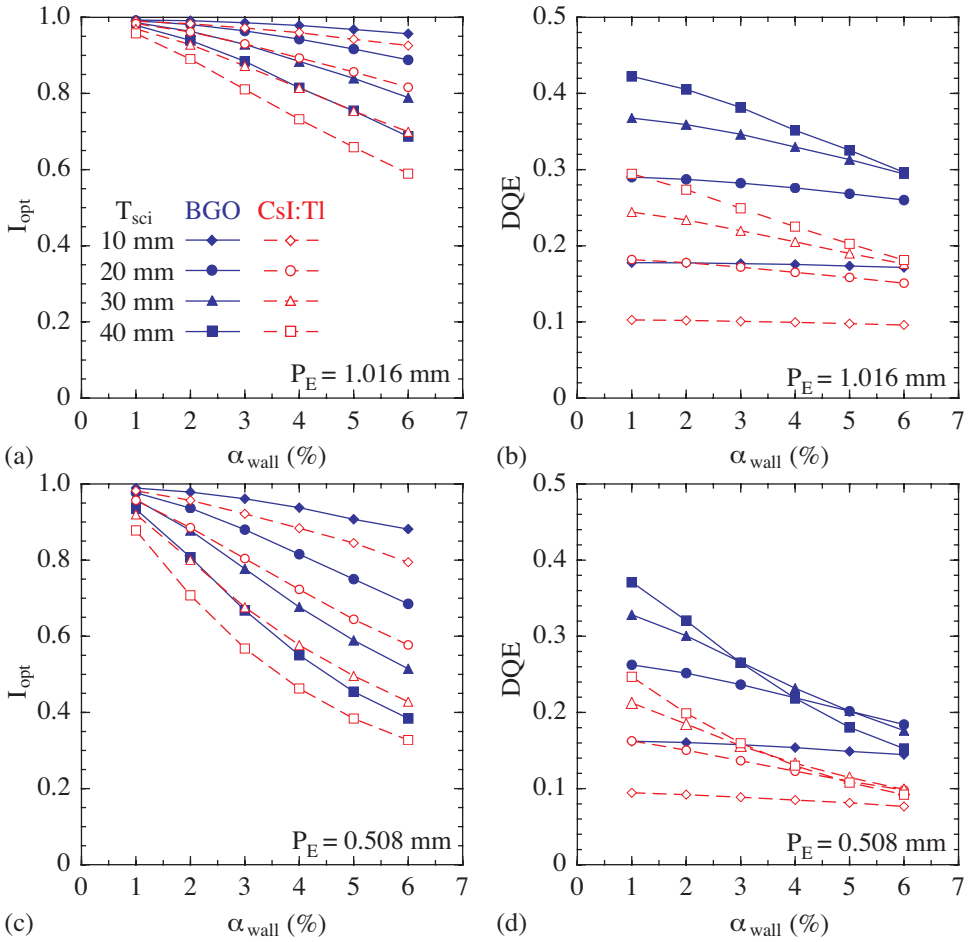

FIG. 7. Simulation results for I_{opt} and DQE plotted as a function of septal wall absorptivity α_{wall} for 10 to 40 mm thick segmented BGO and CsI:Tl detectors. Results for I_{opt} and DQE for detectors with 1.016 mm pitch are shown in (a) and (b), while results for detectors with 0.508 mm pitch are shown in (c) and (d), respectively.

approximately linearly with increasing α_{top}. This decline is explained in the discussion of the results for Fig. 8. Moreover, I_{opt} for each BGO configuration is higher than that for its CsI:Tl counterpart. The same trends were also found for the 10 and 30 mm thick detectors, the results for which are not shown. In addition, for the configurations illustrated in Fig. 6, the effect of α_{top} on DQE (which is not shown) is relatively small (i.e., less than ~0.017).

III.C.3. Absorption at septal walls

Figure 7 illustrates simulation results for I_{opt} and DQE as a function of α_{wall} for 10 to 40 mm thick segmented BGO and CsI:Tl detectors at pitches of 1.016 and 0.508 mm. In these simulations, α_{top} and θ_{max} were chosen to be 100% and 0°, respectively. The results shown in Figs. 7(a) and 7(c) indicate that, for all examined detector designs, I_{opt} decreases as α_{wall} increases. Moreover, this decline is more significant for detectors with greater T_{sci} and smaller P_E, the reason for which is explained in the discussion of the Fig. 8 results below. In addition, I_{opt} for each BGO configuration is higher than that for its CsI:Tl counterpart. Also, as shown in Figs. 7(b) and 7(d), DQE generally decreases with increasing α_{wall}. Moreover, this decrease is more pronounced for detectors with greater T_{sci} and smaller P_E, diminishing the advantage of increasing scintillator thickness. In addition, at pitches of 1.016 and 0.508 mm, the DQE is not strongly affected by increasing α_{wall} for detectors thinner than ~20 and ~10 mm, respectively (at least up to an α_{wall} value of 6%). Finally, at both pitches and at a given value of α_{wall}, the 20 mm thick BGO detector generally provides higher DQE than CsI:Tl detectors up to 40 mm thick.

The results shown in Figs. 7(a) and 7(c) demonstrate that I_{opt} decreases with higher α_{wall}, greater T_{sci}, and smaller P_E. As indicated by Eq. (2), greater T_{sci} and smaller P_E both result in greater ϕ_{sci}. In order to examine the combined influence of ϕ_{sci} and α_{wall} on I_{opt}, results for segmented BGO and CsI:Tl detectors configured with an absorptive and a reflective top reflector are plotted as a function of $\phi_{sci} \times \alpha_{wall}$ in Fig. 8. The four sets of simulation results include some of the results illustrated in Figs. 6 and 7. In addition, the two sets of results for the reflective top reflector also include results obtained from simulations performed at a value of α_{wall} equal to 4%. In all simulations, θ_{max} was assumed to be 0°. For a given set of results, the small difference in I_{opt} observed for simulation results that correspond to the same value of $\phi_{sci} \times \alpha_{wall}$ is a consequence of the competing, nonlinear effects of ϕ_{sci} and α_{wall} on I_{opt} when there is optical absorption in the scintillator crystals (i.e., when $\mu_{A\text{-sci}}$ is not equal to 0 cm^{-1}). For example, at a value of 1.75 for $\phi_{sci} \times \alpha_{wall}$, the detector configuration with a greater T_{sci}, the same P_E, but smaller α_{wall} shows slightly lower I_{opt}. For the smallest examined value of $\phi_{sci} \times \alpha_{wall}$, ~0.1, I_{opt} is greater

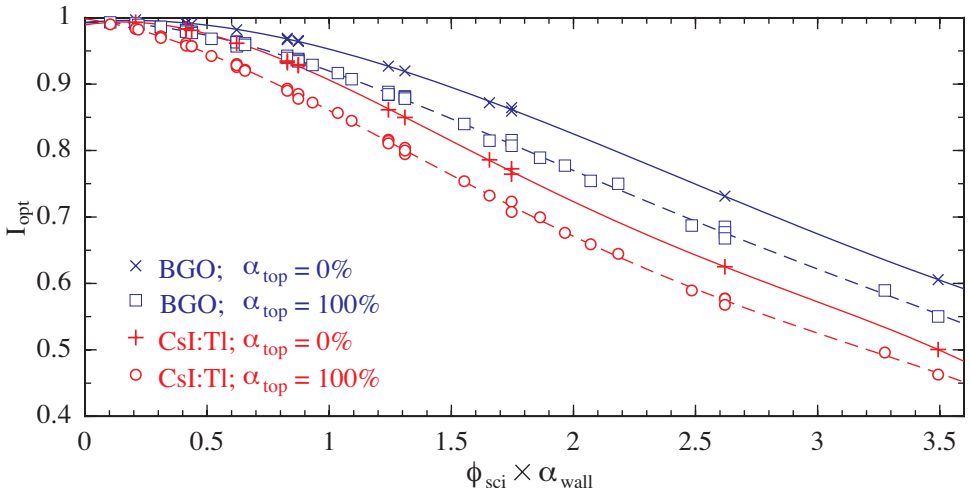

FIG. 8. Simulation results for I_{opt} plotted as a function of the product of the aspect ratio of the scintillator crystals, ϕ_{sci}, and α_{wall}. Results are shown for AMFPIs employing segmented BGO or CsI:Tl detectors configured with a reflective (α_{top} equal to 0%) or an absorptive (α_{top} equal to 100%) top reflector. The solid and dashed lines correspond to fits to the simulation results using fourth order polynomial functions.

than 0.99 for all four sets of simulations. As $\phi_{sci} \times \alpha_{wall}$ increases, I_{opt} declines in all cases mainly due to increased optical absorption at the septal walls. Specifically, greater ϕ_{sci} increases the number of optical interactions occurring at the walls, whereas higher α_{wall} increases the chance of absorption for each interaction event. For a given top reflector absorptivity, BGO offers higher I_{opt} compared to CsI:Tl at the same value of $\phi_{sci} \times \alpha_{wall}$. This difference initially increases as $\phi_{sci} \times \alpha_{wall}$ increases but remains approximately constant beyond a $\phi_{sci} \times \alpha_{wall}$ value of ~1.9. For a given scintillator material, the I_{opt} obtained with a reflective top reflector is higher than that obtained with an absorptive top reflector. Initially, this difference increases with increasing $\phi_{sci} \times \alpha_{wall}$ but does not further increase beyond $\phi_{sci} \times \alpha_{wall}$ values of ~1.9 and 1.1 for BGO and CsI:Tl, respectively. For both BGO and CsI:Tl, this difference remains less than ~0.06 for $\phi_{sci} \times \alpha_{wall}$ values up to ~3.5.

III.C.4. Scattering at the side surfaces of the scintillator crystals

Figure 9 shows simulation results for I_{opt} and DQE as a function of θ_{max} for 10 to 40 mm thick segmented BGO and CsI:Tl detectors at pitches of 1.016 and 0.508 mm. In these simulations, α_{top} and α_{wall} were assumed to be 100% and 2%, respectively. As shown in Figs. 9(a) and 9(c), I_{opt} decreases with increasing θ_{max}, except between 0° and 5°, where a slight increase is observed for some of the 10 and 20 mm thick detectors. Moreover, those detectors with greater T_{sci} and smaller P_E are more affected by increasing θ_{max}. In addition, although each BGO detector offers higher I_{opt} than its CsI:Tl counterpart at θ_{max} equal to 0°, this difference is reduced and, for thicker detectors, reversed as θ_{max} increases. In particular, the reversal of this difference occurs at progressively smaller θ_{max} values for detectors with greater T_{sci} and smaller P_E. As shown in Figs. 9(b) and 9(d), DQE generally decreases with increasing θ_{max} and this decrease is more significant for detectors with greater T_{sci} and smaller P_E, diminishing the DQE advantage of increasing scintillator thickness. In addition, at pitches of 1.016 and 0.508 mm, the DQE for detectors thinner than ~20 and ~10 mm, respectively, is not significantly affected by increasing θ_{max} (at least up to θ_{max} values of 20°). Finally, at both pitches and for a given value of θ_{max}, the 20 mm thick BGO detectors provide higher DQE than CsI:Tl detectors up to 40 mm thick.

The results shown in Figs. 9(b) and 9(d) demonstrate that, for all the detector designs examined, the decline of DQE with increasing θ_{max} is not steep at small values of θ_{max}. For purposes of this study, the θ_{max} value at which DQE drops to 90% of its value at θ_{max} equal to 0° is defined as the roughness resistance of the scintillator crystal side surfaces, $\theta_{max-0.9}$. In Fig. 10, values for $\theta_{max-0.9}$ are plotted as a function of T_{sci} for BGO and CsI:Tl detectors at pitches of 1.016 and 0.508 mm. In the figure, $\theta_{max-0.9}$ is seen to decrease in an asymptotic-like manner as T_{sci} increases. Moreover, at a given T_{sci}, $\theta_{max-0.9}$ is significantly higher for those detectors with the larger pitch. In addition, at the larger pitch, each BGO detector offers a higher value of $\theta_{max-0.9}$ than its CsI:Tl counterpart. By comparison, at the smaller pitch, BGO offers higher $\theta_{max-0.9}$ only when T_{sci} is less than ~30 mm.

Figure 11 shows simulation results for I_{opt} as a function of ϕ_{sci} for BGO and CsI:Tl detectors at θ_{max} values of 10° and 20°. The four sets of results shown in this figure were obtained using detector thicknesses varying from 10 to 40 mm and pitches of 0.508, 0.65, 0.8, and 1.016 mm, and include some of the results shown in Fig. 9. In all simulations, α_{top} and α_{wall} were assumed to be 100% and 2%, respectively. For all four sets of simulations, I_{opt} is observed to decrease as ϕ_{sci} increases. At a θ_{max} value of 10°, BGO consistently offers a higher I_{opt} than CsI:Tl. However, at a θ_{max} value of 20°, CsI:Tl provides higher I_{opt} for values of ϕ_{sci} greater than ~40. Note that, no general trends were found when the I_{opt} results for the BGO and CsI:Tl detectors shown in Figs. 9 and 11 were plotted as a function of $\phi_{sci} \times \theta_{max}$.

III.C.5. Comparison of I_{opt} for BGO and CsI:Tl detectors

The simulation results reported in Secs. III C 2 through III C 4 indicate that, at a θ_{max} value of 0°, BGO detectors offer higher I_{opt} than their CsI:Tl counterparts. However, as θ_{max} increases, the difference in I_{opt} between the BGO and

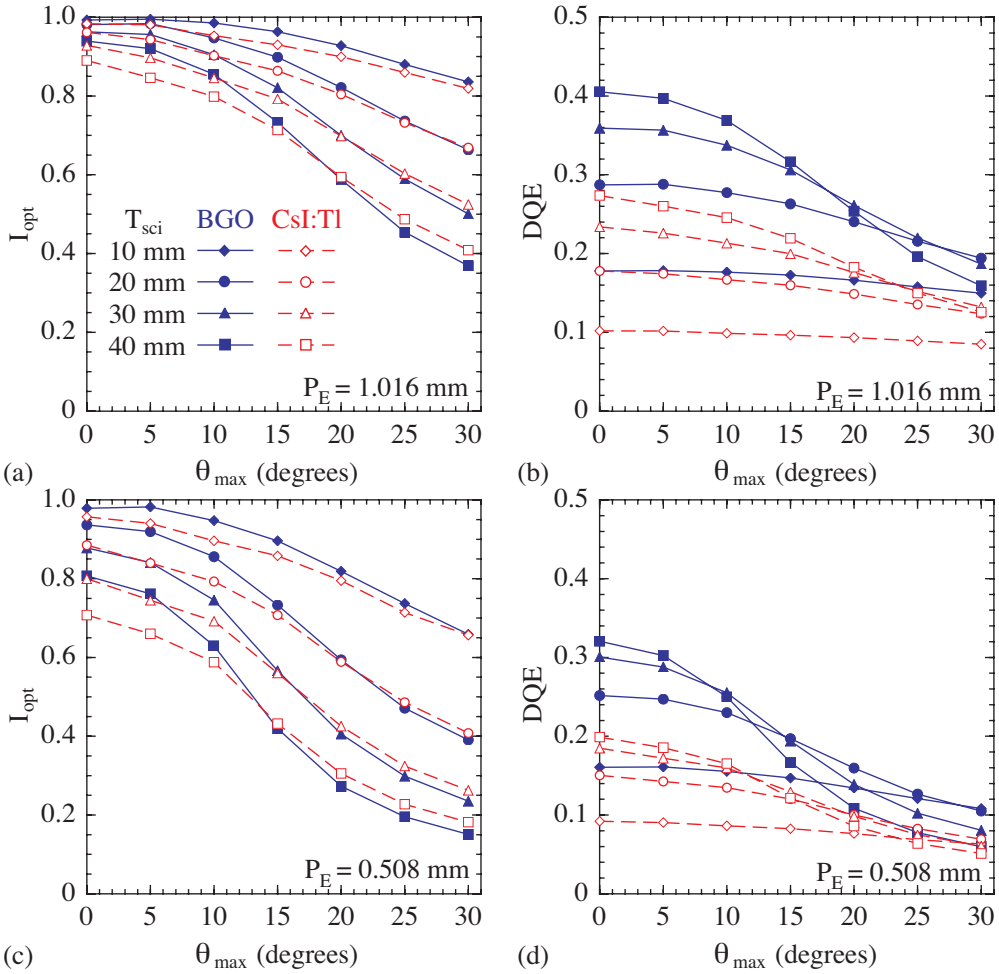

FIG. 9. Simulation results for I_{opt} and DQE as a function of the roughness of the side surfaces scintillator crystals, θ_{max}, for 10 to 40 mm thick segmented BGO and CsI:Tl detectors. Results for I_{opt} and DQE for detectors with 1.016 mm pitch are shown in (a) and (b), while results for detectors with 0.508 mm pitch are shown in (c) and (d), respectively.

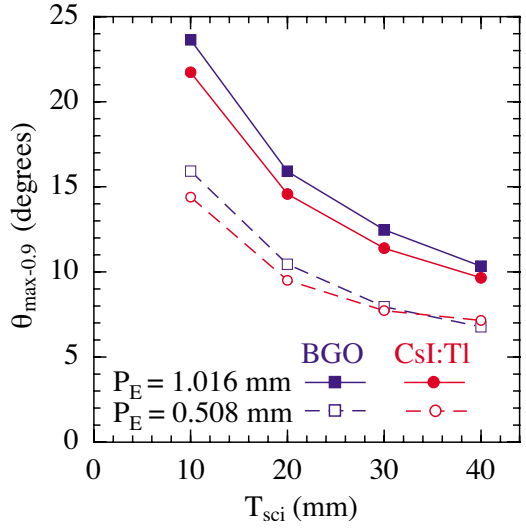

FIG. 10. Results for the roughness resistance, $\theta_{max-0.9}$, of the scintillator crystal side surfaces as a function of T_{sci}. Results, shown for 10 to 40 mm thick segmented BGO and CsI:Tl detectors at pitches of 1.016 and 0.508 mm, were obtained from the I_{opt} results appearing in Fig. 9.

CsI:Tl detectors is reduced and, for thicker detectors, is eventually reversed. It is believed that this complex behavior is the result of the higher refractive index of BGO, 2.15, compared to that of CsI:Tl, 1.79. Since the refractive index of the photodiode array, 1.70, is lower than that of both scintillators, total internal reflection occurs at the bottom surface of the scintillator crystals starting at critical angles γ of 52° and 72° for the BGO and CsI:Tl detectors, respectively. As a result of these different γ values, light photons incident at angles between 52° and 72° can be detected for the CsI:Tl detectors but not for the BGO detectors. For the case of θ_{max} equal to 0°, these photons, compared to those incident at angles smaller than 52°, have traveled through pathways that are less perpendicular to the photodiode array. On average, they have experienced more interactions at the partially absorptive septal walls. The detection of these additional photons results in widening of the optical pulse distribution, reducing I_{opt} for the CsI:Tl detectors. However, as θ_{max} increases, the aforementioned correlation between a photon's incident angle on the bottom surface of the scintillator crystals and the number of interactions it incurs is weakened, which reduces the difference in I_{opt} between the BGO and

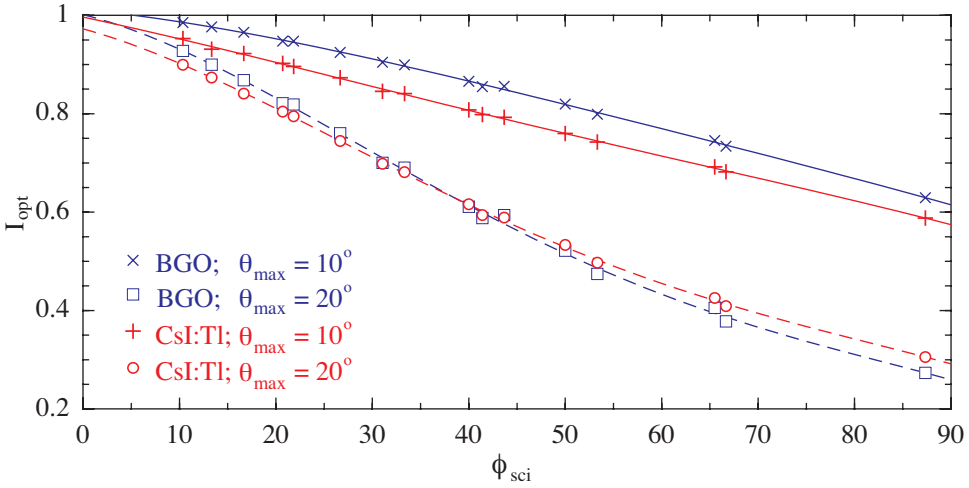

FIG. 11. Simulation results for I_{opt} as a function of ϕ_{sci} for BGO and CsI:Tl detectors at θ_{max} values of 10° and 20°. The solid and dashed lines correspond to fits to the simulation results using fourth order polynomial functions.

CsI:Tl detectors. In the case of larger θ_{max} values, CsI:Tl has the advantage of a higher mean value for the optical pulse distribution, resulting in slightly higher I_{opt} as observed in Figs. 9 and 11.

IV. DISCUSSION AND CONCLUSIONS

The theoretical investigation of optical Swank noise and DQE reported in this article illustrates how Monte Carlo techniques can be used to explore the numerous parameter choices involved in the design of segmented scintillating detectors so as to achieve optimized prototypes that provide greatly improved DQE compared to conventional MV AMFPIs. Such techniques allow examination of Swank noise contributions originating from both optical and radiation transport. In the present study, the Swank noise due to the 6 MV poly-energetic x-ray spectrum and the Swank noise resulting from the absorbed energy distributions are combined in the AEDs, resulting in the combined radiation Swank factor I_{rad}. As shown in Fig. 3(b), I_{rad} is on the order of 0.5, causing the DQE to decrease by approximately a factor of 2. Additional degradation can occur if the optical properties of the scintillator crystals and the septal walls are not carefully chosen. The effect of these properties on DQE is quantified by the optical Swank factor I_{opt}. The simulation results reported in Sec. III demonstrate that I_{opt} is larger for detectors with smaller ϕ_{sci} (i.e., smaller T_{sci} and larger P_E). Although the use of larger P_E leads to higher DQE at zero spatial frequency, it is also necessary to ensure that the element pitch is sufficiently small to avoid significant loss of spatial resolution and DQE at high spatial frequencies. At a given value of ϕ_{sci}, I_{opt} generally decreases with increasing $\mu_{A\text{-}sci}$, $\mu_{S\text{-}sci}$, α_{top}, α_{wall}, or θ_{max}. Among these five optical properties, only α_{wall} and θ_{max} significantly degrade DQE at ϕ_{sci} values greater than ~20 – such as for 10 and 20 mm thick detectors at P_E values of 0.508 and 1.016 mm, respectively. In addition, the results shown in Figs. 7 and 9 can be used to determine the value of α_{wall} and θ_{max} beyond which a thicker detector does not provide a higher DQE. For example, for BGO detectors at a pitch of 0.508 mm, DQE does not increase as T_{sci} increases from 30 to 40 mm when α_{wall} is greater than ~3% (when θ_{max} is equal to 0°) or when θ_{max} is larger than ~8° (when α_{wall} is equal to 2%).

At θ_{max} equal to 0°, the results shown in Fig. 8 (and the corresponding fits) can be used to estimate I_{opt} for detectors having values of T_{sci}, P_E, and α_{wall} that are not specifically examined in this study. Note that such estimates may not be valid beyond the parameter ranges examined in this study. Moreover, since the results in Fig. 6 indicate that I_{opt} decreases approximately linearly with increasing α_{top}, the Fig. 8 results can also be used to estimate I_{opt} for α_{top} values between 0% and 100%. In addition, at θ_{max} of 10° and 20°, the results illustrated in Fig. 11 (and the corresponding fits) can be used to estimate I_{opt} for detectors having values of T_{sci} and P_E that are within the examined range of parameters but not specifically investigated in this study. Finally, in the development of future prototype detectors, the $\theta_{max-0.9}$ values shown in Fig. 10 could provide guidance for avoiding significant loss of DQE due to scattering at the side surfaces of the scintillator crystals.

The examination of hypothetical detector designs reported in Sec. III assumes the use of polystyrene septal walls that have radiation properties generally consistent with the type of polymer walls used in recent prototype detectors.[16,35] Alternatively, septal walls could conceivably be made of metal (e.g., silver foil or tungsten powder with reflective coating). In radiation simulations carried out for BGO and CsI:Tl detectors involving 0.05 mm thick tungsten septal walls, the replacement of polymer walls with tungsten walls was found to result in higher DQE_{rad} – by up to ~0.04 and 0.08 at P_E values of 1.016 and 0.508 mm, respectively. However, metal walls are typically more absorptive (e.g., α_{wall} is greater than 10%) than polymer walls, resulting in lower I_{opt} that may mitigate the higher levels of DQE_{rad}. Were it possible to produce metal walls with low absorptivity, the I_{opt} behaviors reported in Sec. III should also be applicable to detectors employing such walls.

It has also been suggested that metal walls having higher than desired absorptivity could be used if these walls were fabricated so as to exhibit graded absorptivity.[16] Such walls

would be made to provide less optical absorption near the top of the detector (i.e., on the side near the x-ray source) compared to the bottom (i.e., on the side next to the array) – which could potentially improve I_{opt}. As an initial test of this hypothesis, a 40 mm thick CsI:Tl detector was simulated with dual-grade septal walls – such that the absorptivity of the top half of the walls, $\alpha_{wall\text{-}1}$, was fixed at 10%, while that of the bottom half, $\alpha_{wall\text{-}2}$, was fixed at a value ranging from 10% to 14%. The result of these simulations indicates that I_{opt} decreases as $\alpha_{wall\text{-}2}$ increases, showing no gain in I_{opt} for septal walls graded in this manner. However, it is conceivable that, in order to achieve a gain in I_{opt}, the walls need to be divided into many more grades, with optimized absorptivity applied to each grade, or varied in a continuous manner. Simulations to guide the optimization of such graded walls are of interest but are beyond the scope of the present study.

In summary, results from this theoretical investigation suggest that, with optical properties optimized with the help of computer simulations, AMFPIs based on thick, segmented CsI:Tl and BGO detectors offering significantly improved DQE [up to ~29% and 42%, corresponding to ~29 and 42 times higher than that of conventional MV AMFPIs, respectively, as shown in Fig. 7(b)] can be achieved. It is anticipated that such greatly increased DQE will result in significant enhancement of performance for electronic portal imaging and facilitate acquisition of MV CBCT images with soft-tissue visualization at clinically acceptable doses.[9]

ACKNOWLEDGMENTS

The authors would like to thank Dr. Aldo Badano from the U.S. Food and Drug Administration and Dr. Josep Sempau from the Technical University of Catalonia for providing the simulation codes. They also appreciate the information provided by their collaborators at Saint-Gobain Crystals, Dr. Mike Mayhugh, Dr. Peter Menge, and Mr. Lou Perna. The authors would also like to acknowledge Dr. Amit Sawant from Stanford University for his insightful comments. Finally, they thank Dr. Hong Du for helpful comments on the manuscript. This work was supported by NIH Grant No. R01 CA51397.

APPENDIX: JUSTIFICATION FOR REDUCED GAIN IN CsI:Tl SIMULATIONS

This appendix describes the conditions under which, in the present study, a 90% reduction in the conversion gain for CsI:Tl detectors will still lead to a correct determination of I_{opt}. In the MANTIS simulations, an X ray deposits its energy in the scintillator in multiple (k) steps. Each energy deposition, E_k, generates N_k optical photons, as determined by the conversion gain and Eq. (3). For each interacting X ray, the total energy absorbed in the scintillator, E_A, is given by

$$E_A = \sum_k E_k, \tag{A1}$$

while the total number of optical photons generated, N_G, is given by

$$N_G = \sum_k N_k. \tag{A2}$$

Due to light loss in the x-ray detector, only a fraction η of the N_G optical photons are detected in the photodiode array. (η is referred to as the optical detection efficiency.) Therefore, for each interacting X ray, the number of optical photons detected, N_D, is given by

$$N_D = \eta \times N_G, \tag{A3}$$

so that the number of optical photons detected per unit of energy absorbed in the scintillator, N_E, may be determined from

$$N_E = N_D / E_A. \tag{A4}$$

As indicated in Sec. II, the distribution of N_E, $P(N_E)$, referred to as the optical pulse distribution, is used to determine I_{opt} by means of Eqs. (6) and (7). By substituting Eqs. (3) and (A1) to (A3) into Eq. (A4), N_E may be expressed in terms of η, E_k, and G as follows:

$$N_E = \frac{\eta \times \sum_k (\text{Poisson}[\text{round}[E_k \times G]])}{\sum_k E_k}. \tag{A5}$$

Since MANTIS rounds the product $E_k \times G$ to the nearest integer before generating light photons, the use of reduced conversion gain for CsI:Tl (i.e., $G = 0.1 \times G_{CsI:Tl}$) may result in a reduction in N_G greater than the intended 90%. This additional loss in N_G occurs when $0.5 \leq (E_k \times G) < 5$. For this range of $E_k \times G$ values, while the nominal gain will result in generation of a few optical photons (i.e., 1 to 5), the reduced gain will lead to the generation of no light photons (since $E_k \times 0.1 \times G$ is rounded to zero). Therefore, in order to achieve the intended 90% reduction in N_G, the probability of $0.5 \leq (E_k \times G) < 5$ must be negligible.

It is of interest to note that, when the nominal gain for the CsI:Tl detectors is used (i.e., when $G = G_{CsI:Tl}$), N_G is found to be very large (~40 000 to 110 000), resulting in a very small statistical uncertainty for η (~0.3% to 0.5%). This uncertainty remains small (~1.0% to 1.6%) even when N_G is reduced by 90%. Therefore, if N_G is reduced by the intended 90% when reduced gain is used, N_E will also be reduced by ~90% as intended (given that the value of η will remain relatively unchanged). As a result of the reduction in N_E, the first and second order moments of $P(N_E)$, M_1 and M_2, will be reduced to 10% and 1% of their original values, respectively. As can be seen from Eq. (6), since the value of M_0 remains unchanged, the effect of such reductions in M_1 and M_2 will cancel out, leaving the value of I_{opt} unchanged.

In summary, in order to demonstrate the validity of using reduced gain, it is necessary to show that the probability of $0.5 \leq (E_k \times G) < 5$ is not high enough to affect the determination of I_{opt}. For each CsI:Tl detector design (i.e., for a collection of CsI:Tl detector configurations offering the same radiation transport properties and the same value of G), such validation can be demonstrated by comparing I_{opt} values determined from simulations using the nominal and reduced

gains. This comparison only needs to be performed for one configuration of each design, since the value of $E_k \times G$ is the same for all configurations of that design.

[a]Electronic mail: wangyi@umich.edu
[b]Author to whom correspondence should be addressed. Electronic mail: antonuk@umich.edu; Telephone: (734) 936-4312; Fax: (734) 936-2261.

[1]L. E. Antonuk, "Electronic portal imaging devices: A review and historical perspective of contemporary technologies and research," Phys. Med. Biol. **47**, R31–R65 (2002).
[2]J. Pouliot, A. Bani-Hashemi, J. Chen, M. Svatos, F. Ghelmansarai, M. Mitschke, M. Aubin, P. Xia, O. Morin, K. Bucci, M. Roach 3rd, P. Hernandez, Z. Zheng, D. Hristov, and L. Verhey, "Low-dose megavoltage cone-beam CT for radiation therapy," Int. J. Radiat. Oncol., Biol., Phys. **61**, 552–560 (2005).
[3]Y. El-Mohri, K.-W. Jee, L. E. Antonuk, M. Maolinbay, and Q. Zhao, "Determination of the detective quantum efficiency of a prototype, megavoltage indirect detection, active matrix flat-panel imager," Med. Phys. **28**, 2538–2550 (2001).
[4]L. E. Antonuk, K.-W. Jee, Y. El-Mohri, M. Maolinbay, S. Nassif, X. Rong, Q. Zhao, J. H. Siewerdsen, R. A. Street, and K. S. Shah, "Strategies to improve the signal and noise performance of active matrix, flat-panel imagers for diagnostic x-ray applications," Med. Phys. **27**, 289–306 (2000).
[5]Y. El-Mohri, L. E. Antonuk, Q. Zhao, Y. Wang, Y. Li, H. Du, and A. Sawant, "Performance of a high fill factor, indirect detection prototype flat-panel imager for mammography," Med. Phys. **34**, 315–327 (2007).
[6]P. R. Granfors, R. Aufrichtig, G. E. Possin, B. W. Giambattista, Z. S. Huang, J. Liu, and B. Ma, "Performance of a 41×41 cm^2 amorphous silicon flat panel x-ray detector designed for angiographic and R&F imaging applications," Med. Phys. **30**, 2715–2726 (2003).
[7]A. Sawant, L. E. Antonuk, Y. El-Mohri, Q. Zhao, Y. Li, Z. Su, Y. Wang, J. Yamamoto, H. Du, I. Cunningham, M. Klugerman, and K. Shah, "Segmented crystalline scintillators: An initial investigation of high quantum efficiency detectors for megavoltage x-ray imaging," Med. Phys. **32**, 3067–3083 (2005).
[8]B. A. Groh, J. H. Siewerdsen, D. G. Drake, J. W. Wong, and D. A. Jaffray, "A performance comparison of flat-panel imager-based MV and kV cone-beam CT," Med. Phys. **29**, 967–975 (2002).
[9]Y. Wang, L. E. Antonuk, Y. El-Mohri, Q. Zhao, A. Sawant, and H. Du, "Monte Carlo investigations of megavoltage cone-beam CT using thick, segmented scintillating detectors for soft tissue visualization," Med. Phys. **35**, 145–158 (2008).
[10]H. Keller, M. Glass, R. Hinderer, K. Ruchala, R. Jeraj, G. Olivera, and T. R. Mackie, "Monte Carlo study of a highly efficient gas ionization detector for megavoltage imaging and image-guided radiotherapy," Med. Phys. **29**, 165–175 (2002).
[11]G. Pang and J. A. Rowlands, "Development of high quantum efficiency, flat panel, thick detectors for megavoltage x-ray imaging: a novel direct-conversion design and its feasibility," Med. Phys. **31**, 3004–3016 (2004).
[12]G. Pang, X. Mei, and J. A. Rowlands, "Development of a novel high quantum efficiency flat panel detector for megavoltage cone beam CT/DT: Construction and evaluation of a prototype single-row detector," Med. Phys. **33**, 2281 (2006).
[13]X. Mei, J. A. Rowlands, and G. Pang, "Electronic portal imaging based on Cerenkov radiation: A new approach and its feasibility," Med. Phys. **33**, 4258–4270 (2006).
[14]Q. Zhao, L. E. Antonuk, Y. El-Mohri, H. Du, Y. Li, A. Sawant, Z. Su, Y. Wang, and J. Yamamoto, "High DQE megavoltage imaging using active matrix flat-panel imagers incorporating polycrystalline mercuric iodide," Med. Phys. **32**, 2131 (2005).
[15]A. Sawant, L. E. Antonuk, Y. El-Mohri, Y. Li, Z. Su, Y. Wang, J. Yamamoto, Q. Zhao, H. Du, J. Daniel, and R. A. Street, "Segmented phosphors—MEMS-based high quantum efficiency detectors for megavoltage x-ray imaging," Med. Phys. **32**, 553–565 (2005).
[16]A. Sawant, L. E. Antonuk, Y. El-Mohri, Q. Zhao, Y. Wang, Y. Li, H. Du, and L. Perna, "Segmented crystalline scintillators: Empirical and theoretical investigation of a high quantum efficiency EPID based on an initial engineering prototype CsI(Tl) detector," Med. Phys. **33**, 1053–1066 (2006).
[17]E. J. Morton, W. Swindell, D. G. Lewis, and P. M. Evans, "A linear array, scintillation crystal-photodiode detector for megavoltage imaging," Med. Phys. **18**, 681–691 (1991).
[18]S. Rathee, D. Tu, T. T. Monajemi, D. W. Rickey, and B. G. Fallone, "A bench-top megavoltage fan-beam CT using CdWO4-photodiode detectors. I. System description and detector characterization," Med. Phys. **33**, 1078–1089 (2006).
[19]T. T. Monajemi, D. Tu, B. G. Fallone, and S. Rathee, "A bench-top megavoltage fan-beam CT using CdWO4-photodiode detectors. II. Image performance evaluation," Med. Phys. **33**, 1090–1100 (2006).
[20]M. A. Mosleh-Shirazi, W. Swindell, and P. M. Evans, "Optimization of the scintillation detector in a combined 3D megavoltage CT scanner and portal imager," Med. Phys. **25**, 1880–1890 (1998).
[21]E. J. Seppi, P. Munro, S. W. Johnsen, E. G. Shapiro, C. Tognina, D. Jones, J. M. Pavkovich, C. Webb, I. Mollov, L. D. Partain, and R. E. Colbeth, "Megavoltage cone-beam computed tomography using a high-efficiency image receptor," Int. J. Radiat. Oncol., Biol., Phys. **55**, 793–803 (2003).
[22]T. T. Monajemi, B. G. Fallone, and S. Rathee, "Thick, segmented $CdWO_4$ -photodiode detector for cone beam megavoltage CT: A Monte Carlo study of system design parameters," Med. Phys. **33**, 4567–4577 (2006).
[23]R. K. Swank, "Absorption and noise in x-ray phosphors," J. Appl. Phys. **44**, 4199–4203 (1973).
[24]C. Kausch, B. Schreiber, F. Kreuder, R. Schmidt, and O. Dossel, "Monte Carlo simulations of the imaging performance of metal plate/phosphor screens used in radiotherapy," Med. Phys. **26**, 2113–2124 (1999).
[25]D. A. Jaffray, J. J. Battista, A. Fenster, and P. Munro, "Monte Carlo studies of x-ray energy absorption and quantum noise in megavoltage transmission radiography," Med. Phys. **22**, 1077–1088 (1995).
[26]L. E. Antonuk, Y. El-Mohri, W. Huang, K.-W. Jee, J. H. Siewerdsen, M. Maolinbay, V. E. Scarpine, H. Sandler, and J. Yorkston, "Initial performance evaluation of an indirect-detection, active matrix flat-panel imager (AMFPI) prototype for megavoltage imaging," Int. J. Radiat. Oncol., Biol., Phys. **42**, 437–454 (1998).
[27]A. Badano and J. Sempau, "MANTIS: Combined x-ray, electron and optical Monte Carlo simulations of indirect radiation imaging systems," Phys. Med. Biol. **51**, 1545–1561 (2006).
[28]F. Salvat, J. M. Fernández-Varea, and J. Sempau, PENELOPE, a code system for Monte Carlo simulation of electron and photon transport, 2003.
[29]A. Badano, Ph.D. thesis, University of Michigan, 1999.
[30]Product data sheet for cesium iodide scintillation material, Saint-Gobain Crystals, OH.
[31]Product data sheet for bismuth germanate scintillation material, Saint-Gobain Crystals, OH.
[32]D. Sheikh-Bagheri, Ph.D. thesis, Carleton University, 1999.
[33]I. M. Blevis, D. C. Hunt, and J. A. Rowlands, "X-ray imaging using amorphous selenium: Determination of Swank factor by pulse height spectroscopy," Med. Phys. **25**, 638–641 (1998).
[34]Sait-Gobain Crystals, Ohio (private communication).
[35]Y. Wang, Q. Zhao, L. E. Antonuk, Y. El-Mohri, and M. Koniczek, "Empirical investigation of flat-panel imagers incorporating high-efficiency, segmented BGO and CsI:Tl detectors for radiotherapy imaging," Med. Phys. **35**, 2853 (2008).